JCI The Journal of Clinical Investigation

Hedgehog signaling promotes tumor-associated macrophage polarization to suppress intratumoral CD8$^+$ T cell recruitment

Amy J. Petty, … , Xiaopei Huang, Yiping Yang

J Clin Invest. 2019;129(12):5151-5162. https://doi.org/10.1172/JCI128644.

Research Article **Immunology**

Tumor-associated macrophages (TAMs) usually display an antiinflammatory M2-like phenotype to facilitate tumor growth. However, what drives M2 polarization of TAMs and how TAMs suppress antitumor immunity within the tumor microenvironment (TME) remain largely undefined. Using several murine tumor models, we showed that hedgehog (Hh) signaling in myeloid cells is critical for TAM M2 polarization and tumor growth. We also found that tumor cells secrete sonic hedgehog (SHH), an Hh ligand, and that tumor-derived SHH drives TAM M2 polarization. Furthermore, Hh-induced functional polarization in TAMs suppresses CD8$^+$ T cell recruitment to the TME through the inhibition of CXCL9 and CXCL10 production by TAMs. Last, we demonstrated that Krüppel-like factor 4 (Klf4) mediates Hh-dependent TAM M2 polarization and the immunosuppressive function. Collectively, these findings highlight a critical role for tumor-derived SHH in promoting TAM M2 polarization, a mechanism for TAM-mediated immunosuppression, and may provide insights into the design of new cancer immunotherapeutic strategies.

Hedgehog signaling promotes tumor-associated macrophage polarization to suppress intratumoral CD8+ T cell recruitment

Amy J. Petty,[1,2] Ang Li,[2] Xinyi Wang,[1,2] Rui Dai,[1,2] Benjamin Heyman,[2] David Hsu,[2] Xiaopei Huang,[2] and Yiping Yang[2,3]

[1]Department of Pharmacology and Cancer Biology, [2]Division of Hematologic Malignancies and Cellular Therapy, Department of Medicine, and [3]Department of Immunology, Duke University, Durham, North Carolina, USA.

Tumor-associated macrophages (TAMs) usually display an antiinflammatory M2-like phenotype to facilitate tumor growth. However, what drives M2 polarization of TAMs and how TAMs suppress antitumor immunity within the tumor microenvironment (TME) remain largely undefined. Using several murine tumor models, we showed that hedgehog (Hh) signaling in myeloid cells is critical for TAM M2 polarization and tumor growth. We also found that tumor cells secrete sonic hedgehog (SHH), an Hh ligand, and that tumor-derived SHH drives TAM M2 polarization. Furthermore, Hh-induced functional polarization in TAMs suppresses CD8+ T cell recruitment to the TME through the inhibition of CXCL9 and CXCL10 production by TAMs. Last, we demonstrated that Krüppel-like factor 4 (Klf4) mediates Hh-dependent TAM M2 polarization and the immunosuppressive function. Collectively, these findings highlight a critical role for tumor-derived SHH in promoting TAM M2 polarization, a mechanism for TAM-mediated immunosuppression, and may provide insights into the design of new cancer immunotherapeutic strategies.

Introduction

Macrophages play an important role in a variety of cellular functions ranging from tissue homeostasis to development (1). They demonstrate great functional plasticity depending on environmental cues and can be polarized to 2 distinctive phenotypes — the proinflammatory M1 phenotype and the antiinflammatory M2 phenotype (2, 3). M1 macrophages are activated in response to lipopolysaccharides and IFN-γ, whereas the M2 phenotype can be induced with IL-4/IL-13, IL-10, TGF-β, and macrophage colony-stimulating factor (M-CSF) (2, 3). Similarly, macrophages within tumors (tumor-associated macrophages [TAMs]) have been shown to have key homeostatic functions that influence tumor maintenance and growth (4). Most TAMs within the tumor microenvironment (TME) exhibit an M2-like phenotype and promote tumor growth and metastasis via different mechanisms (4–8). Increased presence of TAMs is correlated with poorer clinical outcome in patients with various types of cancer (9–13). Although a recent study suggested a role for lactic acid in functional polarization of TAMs (14), what promote(s) M2 polarization of TAMs in vivo and how TAMs suppress antitumor immunity within the TME remain largely undefined.

The hedgehog (Hh) pathway is one of the most important signaling pathways in cancer (15). Upon secretion by cells, the Hh family of signaling proteins — Sonic hedgehog (SHH), Desert hedgehog (DHH), and Indian hedgehog (IHH) — bind to the Patched-1 (PTCH1) receptor on adjacent target cells, thereby releasing the suppression of Smoothened (Smo), ultimately resulting in the activation and nuclear translocation of Gli transcription factor members and upregulation of Hh target genes (16). Although the role of autocrine signaling of Hh has been well established in basal cell carcinoma and medulloblastoma (17), the importance of paracrine communications between Hh-secreting tumor cells and stromal cells in promoting tumor growth has only begun to emerge. Recent studies have shown that Hh ligands secreted from a subset of epithelial cancers, including breast, ovarian, colorectal, and pancreatic cancers, can modulate the stromal cells to create a favorable environment to foster cancer progression (18–20). However, it remains to be elucidated how Hh ligands act on stromal cells within the TME to promote tumor growth and what cell type(s) are involved in this process.

In this study, we found using various murine tumor models that Hh signaling in myeloid cells drives M2 polarization of TAMs in tumor stroma to promote tumor growth. We further showed that tumor-derived SHH directly acts on TAMs to promote M2 polarization, mediated by the transcription factor Krüppel-like factor 4 (Klf4). Abrogation of Hh communication between tumor cells and TAMs interferes with TAM M2 polarization and results in stunted tumor growth. Furthermore, we demonstrated that Hh-dependent M2 polarization of TAMs suppresses CD8+ T cell infiltration into the TME via reduction of CXCL9 and CXCL10. Taken together, these findings identify an important role for tumor-derived SHH in promoting M2 polarization of TAMs, a mechanism underlying TAM-mediated immunosuppression, and may provide important insights into the development of novel immunotherapeutic strategies for treating cancer.

Conflict of interest: The authors have declared that no conflict of interest exists.

Submitted: March 6, 2019; **Accepted:** August 20, 2019; **Published:** October 22, 2019.
Reference information: *J Clin Invest*. 2019;129(12):5151–5162.
https://doi.org/10.1172/JCI128644.

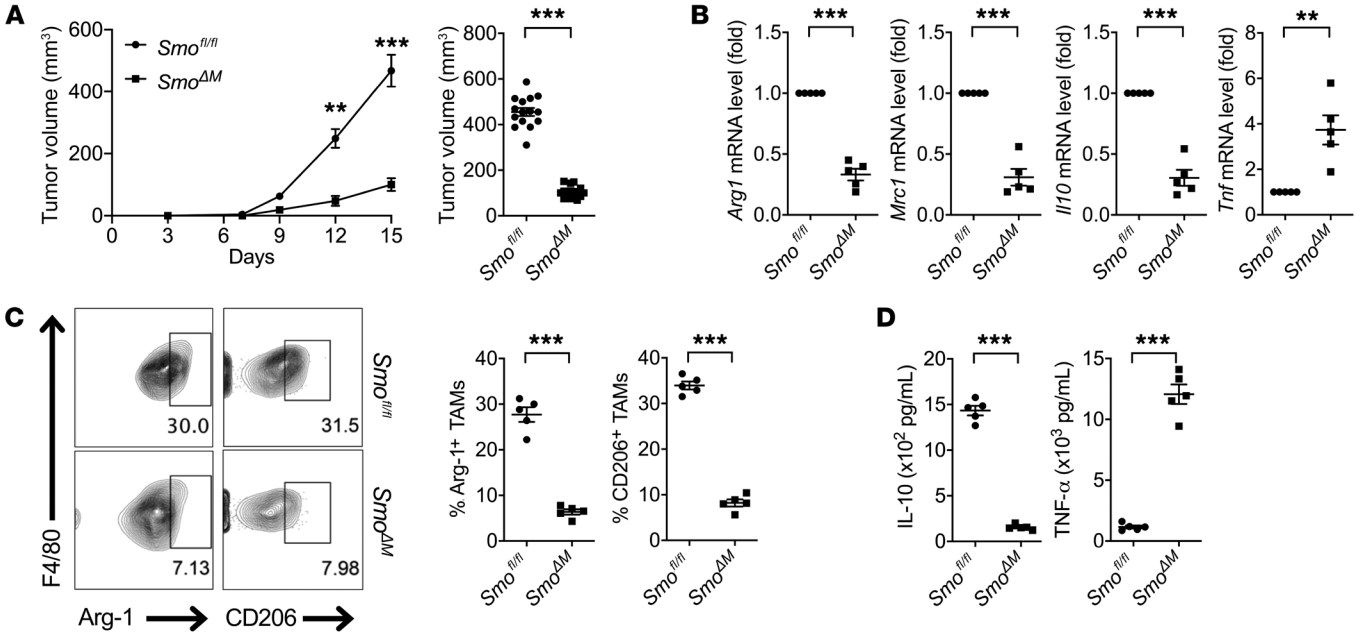

Figure 1. Loss of *Smo* in myeloid cells interferes with tumor growth and M2 polarization of TAMs in vivo. (**A**) Tumor growth of Hepa1-6 mouse hepatoma cells inoculated s.c. in $Smo^{fl/fl}$ and $Smo^{\Delta M}$ mice. Tumor volumes on day 15 at sacrifice are shown. (**B**) *Arg1*, *Mrc1*, *Il10*, and *Tnf* mRNA levels in $Smo^{fl/fl}$ and $Smo^{\Delta M}$ TAMs were measured by qRT-PCR. Expression of mRNAs was normalized to *Actb* and compared with that of $Smo^{fl/fl}$. (**C**) Surface CD206 expression and intracellular Arg-1 production in $Smo^{fl/fl}$ and $Smo^{\Delta M}$ TAMs by FACS. (**D**) TNF-α and IL-10 secretion from $Smo^{fl/fl}$ and $Smo^{\Delta M}$ TAMs was measured by ELISA. Values are mean ± SEM of a minimum of 3 independent experiments. $^{**}P < 0.005$; $^{***}P < 0.0005$. $n = 15$ mice per group (**A**); $n = 5$ biological replicates per group (**B**–**D**). Wilcoxon-Mann-Whitney *U* test (**A**); 2-tailed Student's *t* test (**B**–**D**).

Results

Hh signaling in myeloid cells is important for tumor growth and M2 polarization of TAMs. To determine whether Hh signaling in TAMs plays a role in tumorigenesis, we used a conditional knockout mouse model that allows for myeloid-lineage deletion of *Smo*. We first bred *Smo*-floxed ($Smo^{fl/fl}$) mice that possess *loxP* sites flanking exon 1 of the *Smo* gene (21) to *LysMcre* mice that express Cre recombinase in myeloid cells including macrophages, monocytes, and granulocytes (22), and the resultant $LysMcre^{+}Smo^{fl/fl}$ mice (referred to herein as $Smo^{\Delta M}$) have the *Smo* gene conditionally deleted in these cells. We inoculated 3×10^6 Hepa1-6 murine hepatocellular carcinoma (HCC) cells s.c. into these mice and monitored for tumor growth. At day 15, we found that tumor grew rapidly in the control $Smo^{fl/fl}$ mice, but tumor growth was significantly suppressed in $Smo^{\Delta M}$ mice (Figure 1A), suggesting an important role for Hh signaling in myeloid cells for promoting tumor growth.

We next investigated the composition of myeloid cells within the TME and found that $F4/80^{+}CD11b^{+}$ macrophages were the dominant population, making up 72.2% of all myeloid cells, and this number was not impacted by *Smo* deletion (Supplemental Figure 1, A and B; supplemental material available online with this article; https://doi.org/10.1172/JCI128644DS1). We also did not observe any functional difference in $Smo^{fl/fl}$ and $Smo^{\Delta M}$ $CD11b^{+}Ly6G^{+}$ tumor-associated neutrophils (TANs) based on known TAN functional markers (ref. 23 and Supplemental Figure 1C). Additionally, we found that myeloid-specific *Smo* deletion did not impact other myeloid cell numbers, including monocytes and dendritic cells (DCs) in circulation and in the spleen (Supplemental Figure 1D), or antigen-presenting abilities of DCs (Supplemental Figure 1E). Using quantitative reverse transcription PCR (qRT-PCR) and a Gli reporter, we further confirmed active Hh signaling in macrophages and TAMs (Supplemental Figure 2).

We then evaluated whether the loss of Hh signaling affected M2 polarization of TAMs. We found that there was a marked reduction in the expression of the M2 signature markers arginase-1 (Arg-1), CD206 (C-type mannose receptor-1; Mrc1), IL-10, TGF-β1, and chitinase-like 3 (Chil3) (2) and increased levels of three M1 markers, TNF-α, inducible nitric oxide synthase (iNOS/Nos2), and IL-6 (14), in TAMs from $Smo^{\Delta M}$ mice compared with the control $Smo^{fl/fl}$ mice (Figure 1, B–D, and Supplemental Figure 3). Collectively, these results suggest a critical role for Hh signaling in myeloid cells in promoting TAM M2 polarization and tumor growth.

Intrinsic Hh signaling is also critical for M2 polarization of TAMs in an autochthonous tumor. To further examine the role of Hh signaling in M2 polarization of TAMs in a more physiological environment in which HCC normally arises, we used mice deficient in multidrug resistance gene 2 ($Mdr2^{-/-}$) as an autochthonous model of HCC. The murine *Mdr2* gene encodes a P-glycoprotein that is present in high concentration in the bile canalicular membrane of hepatocytes. $Mdr2^{-/-}$ mice are unable to secrete phospholipids into bile, leading to the development of cholestatic hepatitis followed by HCC (24). Considered as a prototype of inflammation-induced autochthonous cancer (25), these mice spontaneously develop HCC through 3 distinct phases: cholestatic hepatitis/dysplasia at the age of 3–4 months, dysplastic nodules (adenoma-like precancerous lesions) at the age of 6–7 months, and eventually HCC with distant metastases at the age of 9–12 months; and by 16 months of age, virtually all $Mdr2^{-/-}$ mice show liver tumors (25, 26). We generated $LysMcre^{+}Smo^{fl/fl}Mdr2^{-/-}$

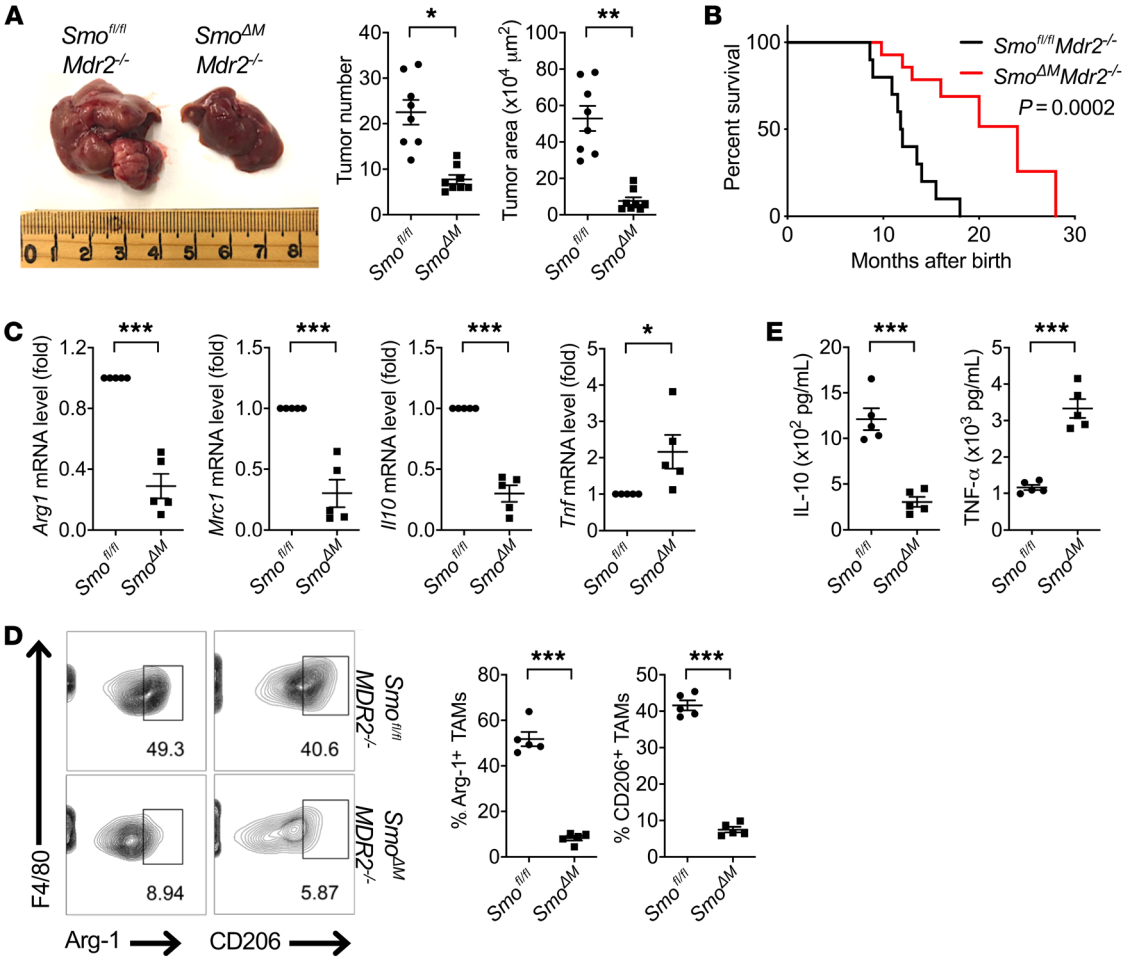

Figure 2. Loss of Hh signaling in myeloid cells suppresses M2 polarization of TAMs and promotes survival in autochthonous HCC. (**A**) Representative gross image of *Smo*$^{fl/fl}$*Mdr2*$^{-/-}$ and *Smo*$^{\Delta M}$*Mdr2*$^{-/-}$ mice at 12 months after birth. Tumor number and tumor area were quantified by counting and measuring of neoplastic nodules per H&E-stained liver sample. (**B**) Kaplan-Meier survival curve for the 2 mouse cohorts, *Smo*$^{fl/fl}$*Mdr2*$^{-/-}$ and *Smo*$^{\Delta M}$*Mdr2*$^{-/-}$. The median survival times were 11.9 months for the *Smo*$^{fl/fl}$*Mdr2*$^{-/-}$ cohort (black line) and 20 months for the *Smo*$^{\Delta M}$*Mdr2*$^{-/-}$ cohort (red line). (**C**–**E**) Expression of Arg-1, CD206 (Mrc1), IL-10, and TNF-α in *Smo*$^{fl/fl}$*Mdr2*$^{-/-}$ and *Smo*$^{\Delta M}$*Mdr2*$^{-/-}$ TAMs was measured by qRT-PCR (**C**), FACS (**D**), and ELISA (**E**). Expression of mRNAs was normalized to *Actb* and compared with that of *Smo*$^{fl/fl}$*Mdr2*$^{-/-}$ TAMs. Values are the mean ± SEM of a minimum of 3 independent experiments. **P* < 0.05; ***P* < 0.005; ****P* < 0.0005. *n* = 8 biological replicates per group (**A**); *n* = 15 mice per group (**B**); *n* = 5 biological replicates per group (**C**–**E**). Two-tailed Student's *t* test (**A** and **C**–**E**); log-rank test (**B**).

mice (referred to as *Smo*$^{\Delta M}$*Mdr2*$^{-/-}$) to study myeloid cell–intrinsic Hh signaling in M2 polarization of TAMs within the TME of HCC. We observed that *Smo*$^{\Delta M}$*Mdr2*$^{-/-}$ mice had a marked reduction in both the number and size of HCC (Figure 2A), leading to a significant ($P < 0.001$) prolongation in survival (median survival = 20 months) compared with that in the control *Smo*$^{fl/fl}$*Mdr2*$^{-/-}$ mice (median survival = 11.9 months) (Figure 2B). Similar to the observations in the Hepa1-6 model, the suppression in tumor growth was associated with a significant reduction in expression of the M2 signature markers Arg-1, CD206, IL-10, TGF-β1, and Chil3, as well as a marked increase in the M1-related markers TNF-α, iNOS, and IL-6 (Figure 2, C–E, and Supplemental Figure 4), in TAMs from *Smo*$^{\Delta M}$*Mdr2*$^{-/-}$ mice. This further supports a critical role for Hh signaling in TAM M2 polarization and HCC development.

Human M2 TAMs express Gli1 in HCC tumors with high SHH activity. To further investigate whether Hh signaling plays a role in human HCC tumorigenesis, we first performed immunohistochemical staining of human HCC tumor with matched healthy liver samples. We found that human HCCs highly express SHH ligands, which was correlated with an increased number of CD163$^+$ M2 TAMs in the TME in comparison with the matched healthy livers (Supplemental Figure 5A). Additionally, immunofluorescent staining of CD163, a human M2 marker, and Gli1 demonstrated that Gli1 colocalized with CD163 (Supplemental Figure 5B), indicating that human M2 TAMs have activation of the Hh signaling pathway. Collectively, these results support that Hh signaling is also active in M2 TAMs human HCC.

Tumor-derived SHH promotes M2 polarization of TAMs in vivo. We next investigated the source of Hh ligands responsible for M2 polarization of TAMs. We hypothesized that tumor-derived Hh ligands are critical in M2 polarization of TAMs. To test this hypothesis, we first examined whether tumor cells produce Hh ligands. Indeed, we found that Hepa1-6 cells secreted a large amount of *Shh*, but not *Ihh* or *Dhh* (Figure 3A). We next showed that addition of recombinant SHH drives M2 polarization of macrophages evidenced by a significant upregulation of the M2-associated mark-

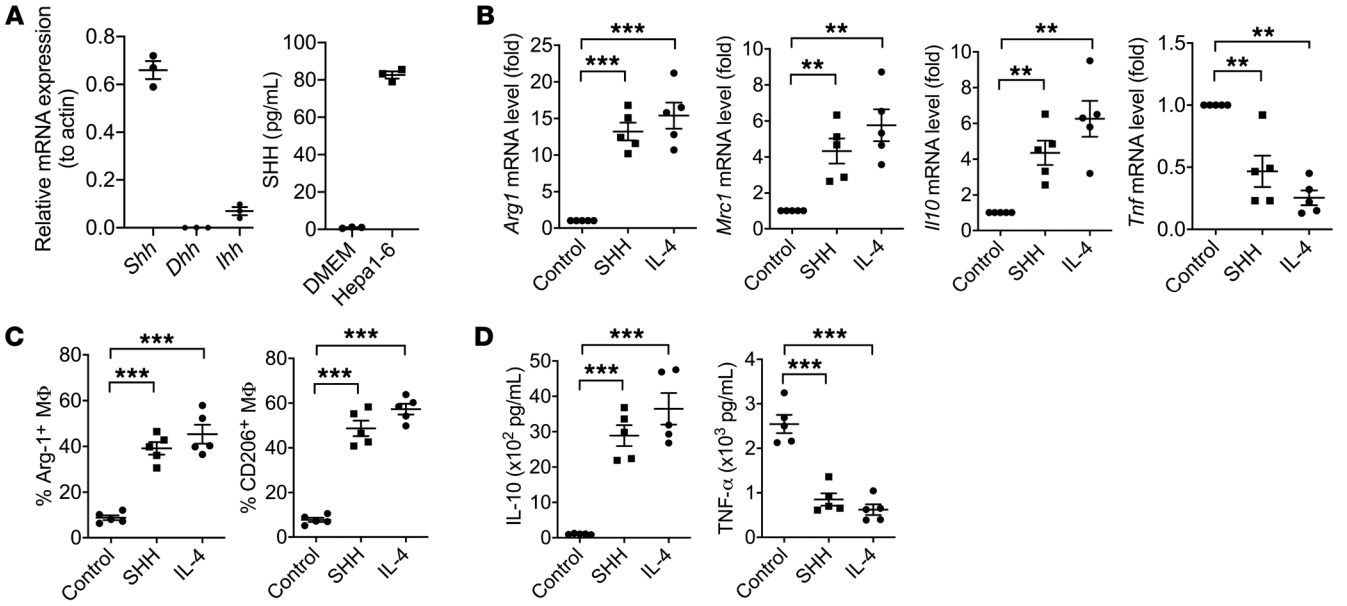

Figure 3. SHH is sufficient to induce M2 polarization of macrophages in vitro. (**A**) *Shh*, *Ihh*, and *Dhh* mRNA levels in Hepa1-6 hepatoma cells were measured by qRT-PCR. Expression was normalized to reference gene *Actb*. Concentration of SHH ligands in Hepa1-6 supernatants and control DMEM was assayed using ELISA. (**B**–**D**) Macrophages (Mφ) from C57BL/6 mice were treated with 100 pg/mL SHH or 100 pg/mL IL-4 for 3 days or left untreated (control). Expression of Arg-1, CD206 (Mrc1), IL-10, and TNF-α in control macrophages and SHH- or IL-4–treated macrophages was measured by qRT-PCR (**B**), FACS (**C**), and ELISA (**D**). Expression of mRNAs was normalized to *Actb* and compared with that of control macrophages (**B**). Values are the mean ± SEM of a minimum of 2 independent experiments. $^{**}P < 0.005$; $^{***}P < 0.0005$. n = 3 technical replicates per group (**A**); n = 5 biological replicates per group (**B**–**D**). One-way ANOVA (**B**–**D**).

ers Arg-1, CD206, IL-10, TGF-β1, and Chil3 and downregulation of the M1 markers TNF-α, iNOS, and IL-6, comparable to the same level induced by IL-4, a known M2 activator (ref. 2, Figure 3, B–D, and Supplemental Figure 6). Collectively, this suggests that SHH is sufficient to induce M2 polarization of macrophages in vitro.

To further investigate the effects of tumor-derived SHH on TAM M2 polarization in vivo, we performed CRISPR/Cas9-mediated knockout of *Shh* in Hepa1-6 as well as in LLC1 (murine Lewis lung carcinoma) cells. Stable *Shh*-KO Hepa1-6 and LLC1 cells were generated by lentiviral transduction and single-cell cloning, while *Shh*-WT controls were transduced with lentivirus expressing a nontargeting sgRNA. Knockout status of *Shh* was confirmed by Western blotting and ELISA (Supplemental Figure 7, A and B). We found that cell proliferation and viability of Hepa1-6 and LLC1 were not affected by the loss of *Shh* via MTT assay (Supplemental Figure 7, C and D). C57BL/6 mice were then inoculated s.c. with 3×10^6 Hepa1-6 *Shh*-WT and *Shh*-KO tumor cells and monitored for tumor growth. We observed that Hepa1-6 *Shh*-WT tumors grew rapidly while *Shh*-KO tumors showed significantly suppressed tumor growth (Figure 4A). In addition, knocking out *Shh* in tumor cells reduced the expression of the M2 markers Arg-1, CD206, IL-10, TGF-β1, and Chil3 in TAMs as measured by qRT-PCR, FACS, and ELISA (Figure 4, B and C, and Supplemental Figure 8), similarly to the reduction in expression of these markers in $Smo^{\Delta M}$ TAMs. Lastly, TAMs isolated from *Shh*-KO tumors produced more TNF-α, iNOS, and IL-6 compared with TAMs from *Shh*-WT tumor samples (Figure 4, B and D, and Supplemental Figure 8). Similar findings were observed with the LLC1 tumor model (Figure 4, E–H, and Supplemental Figure 9). These results demonstrate that tumor-derived SHH plays an important role in promoting TAM M2 polarization and tumor growth in vivo.

Loss of Hh signaling in TAMs promotes CD8⁺ T cell infiltration into the TME via CXCL9 and CXCL10. We next sought to understand how Hh-induced M2 TAM polarization contributes to tumor growth. We assessed the presence of CD8⁺ and CD4⁺ T cells, regulatory T cells (Tregs), and NK cells within the TME of Hepa1-6 tumors from $Smo^{fl/fl}$ versus $Smo^{\Delta M}$ mice by FACS and found that $Smo^{\Delta M}$ tumors showed a 3-fold higher CD8⁺ T cell number compared with $Smo^{fl/fl}$ tumors (Figure 5A and Supplemental Figure 10, A and B). The infiltrating CD8⁺ T cells also demonstrated higher expression of IFN-γ and granzyme B (Supplemental Figure 10C). Loss of Hh signaling did not affect CD4⁺ T cell, Treg, or NK cell numbers (Supplemental Figure 10, D and E). Similarly, CD8⁺ T cell numbers in HCC of $Smo^{\Delta M}Mdr2^{-/-}$ mice showed a 3-fold increase in comparison with tumors derived from $Smo^{fl/fl}Mdr2^{-/-}$ mice (Figure 5B). These results suggest that loss of Hh signaling in TAMs may affect intratumoral CD8⁺ T cell infiltration. Using an in vitro Transwell migration assay, we further showed that migration of activated CD8⁺ T cells toward supernatants of SHH-treated macrophages was significantly reduced compared with the control (Figure 5C). Taken together, these observations suggest that the protumorigenic effect of Hh-induced TAM M2 polarization could be mediated by regulation of the infiltration of CD8⁺ T cells into the TME.

We then proceeded to investigate the mechanism by which Hh-induced M2 TAMs regulate CD8⁺ T cell infiltration into the TME. Given that chemokines play an important role in the recruitment of effector CD8⁺ T cells, we first examined whether

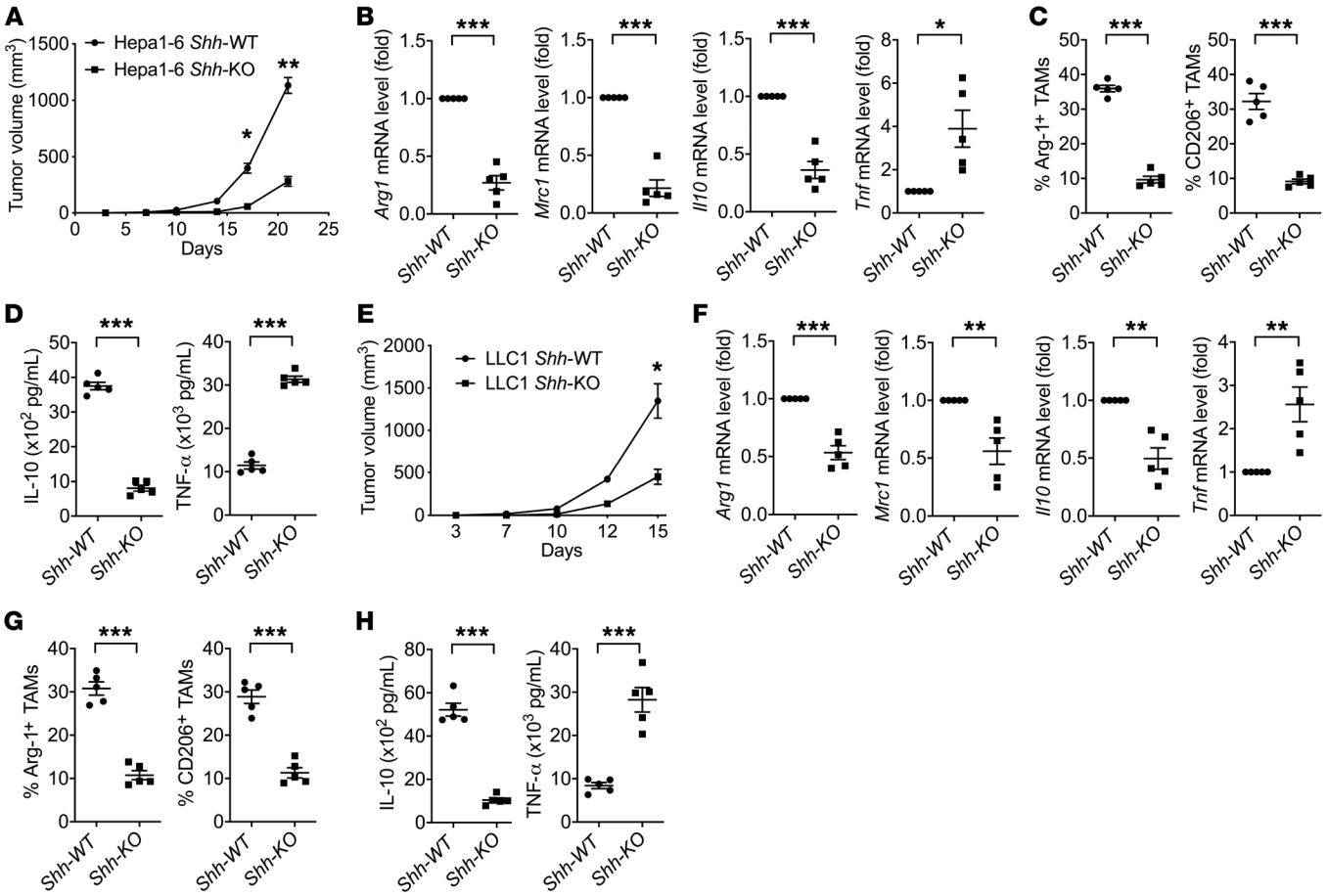

Figure 4. Tumor-derived SHH promotes TAM M2 polarization in vivo. (**A**) Tumor growth of Hepa1-6 *Shh*-WT and Hepa1-6 *Shh*-KO cells inoculated s.c. in C57BL/6 mice. (**B**–**D**) Expression of Arg-1, CD206 (Mrc1), IL-10, and TNF-α in TAMs isolated from Hepa1-6 *Shh*-WT or Hepa1-6 *Shh*-KO tumors was measured by qRT-PCR (**B**), FACS (**C**), and ELISA (**D**). Expression of mRNAs was normalized to *Actb* and compared with that of Hepa1-6 *Shh*-WT TAMs (**B**). (**E**) Tumor growth of LLC1 *Shh*-WT and LLC1 *Shh*-KO cells inoculated s.c. in C57BL/6 mice. (**F**–**H**) Expression of Arg-1, CD206 (Mrc1), IL-10, and TNF-α in TAMs isolated from LLC1 *Shh*-WT or *Shh*-KO tumors was measured by qRT-PCR (**F**), FACS (**G**), and ELISA (**H**). Expression of mRNAs was normalized to *Actb* and compared with that of LLC1 *Shh*-WT TAMs (**F**). Values are the mean ± SEM of a minimum of 3 independent experiments. $^*P < 0.05$; $^{**}P < 0.005$; $^{***}P < 0.0005$. $n = 5$ mice per group (**A**–**H**). Two-tailed Student's *t* test (**B**–**D** and **F**–**H**); Wilcoxon-Mann-Whitney *U* test (**A** and **E**).

SHH treatment alters the IFN-γ–induced expression of *Ccl3*, *Ccl4*, *Ccl5*, *Cxcl9*, and *Cxcl10* in macrophages. We found that *Cxcl9* and *Cxcl10* mRNA levels drastically decreased in the presence of SHH whereas *Ccl3*, *Ccl4*, and *Ccl5* mRNA levels did not vary significantly (Figure 5D). Furthermore, depletion of CXCL9 and CXCL10 resulted in a reduction of 47% and 58% in T cell migration in vitro, respectively (Figure 5E). An 88% reduction in $CD8^+$ T cell migration was observed when CXCL9 and CXCL10 were both depleted, reducing the T cell chemotactic index to a level similar to that observed in the SHH-treated sample (Figure 5E). These data suggest that SHH suppresses $CD8^+$ T cell migration via reduction in CXCL9 and CXCL10 in vitro.

We furthermore showed that $Smo^{\Delta M}$ TAMs exhibited elevated *Cxcl9* and *Cxcl10* mRNA (Figure 5F) and protein (Figure 5G) levels compared with the control $Smo^{fl/fl}$ TAMs. This correlated with our data showing increased $CD8^+$ T cell infiltration in the TME in $Smo^{\Delta M}$ mice (Figure 5A). To address the role of CXCL9 and CXCL10 in $CD8^+$ T cell trafficking in vivo, we used the strategy of CXCR3 blockade, as CXCR3 on $CD8^+$ T cells is the sole chemokine receptor responsible for CXCL9/CXCL10–dependent chemotaxis in C57BL/6 mice (27). $Smo^{fl/fl}$ and $Smo^{\Delta M}$ mice were inoculated s.c. with 3×10^6 Hepa1-6 tumor cells, and mice were injected i.p. with anti-CXCR3 antibodies or isotype controls every 3–4 days. We found that CXCR3 blockade abrogated the suppression of tumor growth we observed in $Smo^{\Delta M}$ mice and promoted tumorigenesis in the $Smo^{\Delta M}$ mice to the level of $Smo^{fl/fl}$ mice (Figure 5H). When we evaluated the percentages and numbers of $CD8^+$ T cells within the TME, we found that blocking CXCR3 in tumor-bearing $Smo^{\Delta M}$ mice reduced $CD8^+$ T cell infiltration to the same level as isotype-injected $Smo^{fl/fl}$ mice (Figure 5, I and J). Collectively, these results suggest that Hh-induced suppression of $CD8^+$ T cell infiltration into the TME is mediated through reduced production of CXCL9 and CXCL10 by TAMs.

Hh-induced TAM M2 polarization and immunosuppressive function are mediated by Klf4. We next investigated how Hh signaling in macrophages promoted their M2 polarization and immunosuppressive function. Previous studies have suggested a panel of transcription factors associated with M2 macrophage polarization, including

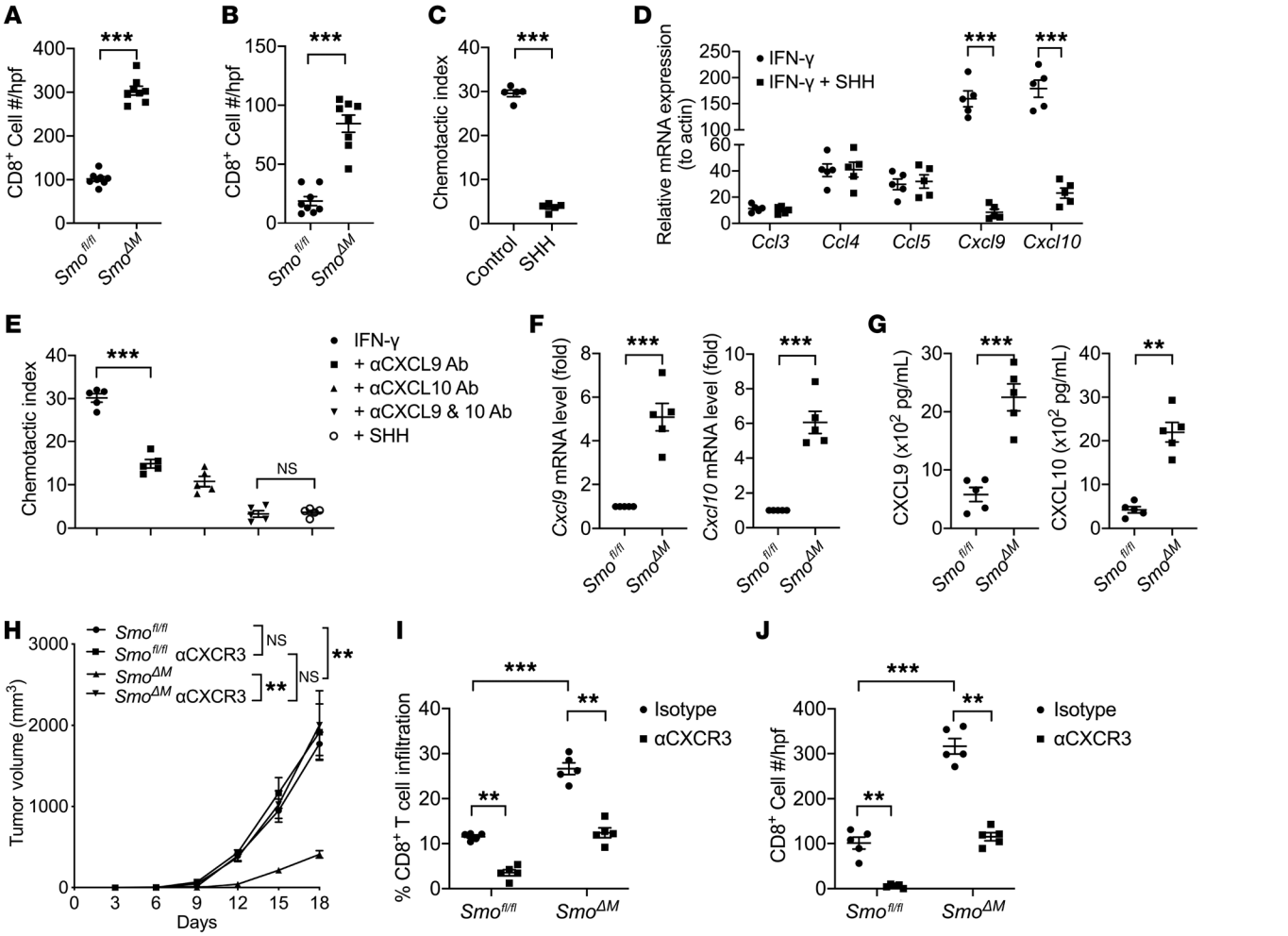

Figure 5. Loss of Hh signaling in TAMs promotes CD8⁺ T cell infiltration via CXCL9 and CXCL10. (**A** and **B**) Quantification of tumor-infiltrating CD8⁺ T cells by immunofluorescent staining in Hepa1-6 cells implanted s.c. into *Smo*$^{fl/fl}$ and *Smo*$^{\Delta M}$ mice (**A**) and in the autochthonous HCC model (**B**). (**C**) Chemotaxis of CD8⁺ T cells toward macrophages treated with IFN-γ (control) and IFN-γ plus SHH. (**D**) *Ccl3*, *Ccl4*, *Ccl5*, *Cxcl9*, and *Cxcl10* mRNA levels in macrophages treated with IFN-γ or with IFN-γ plus SHH were measured by qRT-PCR. Expression was normalized to *Actb* and compared with untreated. (**E**) Chemotaxis of CD8⁺ T cells toward macrophages treated with IFN-γ alone, IFN-γ plus CXCL9 and/or CXCL10-neutralizing antibodies, and IFN-γ plus SHH. (**F** and **G**) Expression of *Cxcl9* and *Cxcl10* in *Smo*$^{fl/fl}$ or *Smo*$^{\Delta M}$ TAMs was measured by qRT-PCR (**F**) and ELISA (**G**). Expression of mRNAs was normalized to *Actb* and compared with that of *Smo*$^{fl/fl}$ TAMs (**F**). (**H**) Tumor growth of Hepa1-6 in *Smo*$^{fl/fl}$ and *Smo*$^{\Delta M}$ mice injected with CXCR3-blocking antibody or isotype control. (**I**) Percentage of tumor CD8⁺ T cell infiltration quantified by FACS. (**J**) Frozen tissue sections were stained for CD8⁺ T cells and quantified under high-power field (hpf). Values are the mean ± SEM of a minimum of 3 independent experiments. $^{**}P < 0.005$; $^{***}P < 0.0005$. *n* = 8 biological replicates per group (**A** and **B**); *n* = 5 technical replicates per group (**C** and **E**); *n* = 5 biological replicates per group (**D**, **F**–**J**). Two-tailed Student's *t* test (**A**–**D**, **F**, and **G**); 1-way ANOVA (**E**); Kruskal-Wallis test (**H**); 2-way ANOVA (**I** and **J**). α, anti.

Klf2, Klf4, Stat6, CEBPβ, and PPARγ (2, 28). Thus, we surveyed the expression levels of these transcription factors in peritoneal macrophages treated with SHH and found that *Klf4* mRNA expression levels were significantly elevated in comparison with untreated control (Figure 6A). We further found that *Klf4* mRNA levels were significantly reduced in *Smo*$^{\Delta M}$ TAMs compared with *Smo*$^{fl/fl}$ TAMs (Figure 6B), suggesting that Klf4 could be mediating the downstream effects of SHH in M2 macrophage polarization. Through in silico promoter analysis, we found a consensus Gli-binding sequence (GCCCCGCCCC) (29) at the –221 to –211 position upstream of the transcription start site of the *Klf4* gene. Using the ChIP method, we were able to demonstrate Gli1 occupancy at that site when macrophages were treated with SHH or had constitutive activation of *Smo*, referred to as *Smo*^{CM} (ref. 30 and Figure 6C). Furthermore, such binding was not observed when macrophages were treated with GANT61, a small-molecule inhibitor of Gli transcription factors (31), or when *Smo* was deleted in macrophages (Figure 6C). This confirms that Gli1 transcriptionally regulates *Klf4* in macrophages and suggests that Klf4 could be mediating the downstream effects of SHH in M2 macrophage polarization.

To further address this question, we first generated *LysMcre*⁺ *Klf4*$^{fl/fl}$ (referred to as *Klf4*$^{\Delta M}$) mice with *Klf4* deleted in myeloid cells (32). After being inoculated with SHH-secreting Hepa1-6 tumor cells, *Klf4*$^{\Delta M}$ mice exhibited reduced tumor growth when inoculated with Hepa1-6 cells, compared with *Klf4*$^{fl/fl}$ mice (Figure 6D). Such reduction in tumor growth was correlated with decreased expression of the M2 markers Arg-1, CD206, IL-10, TGF-β1, and Chil3 in TAMs (Figure 6E and Supplemental Fig-

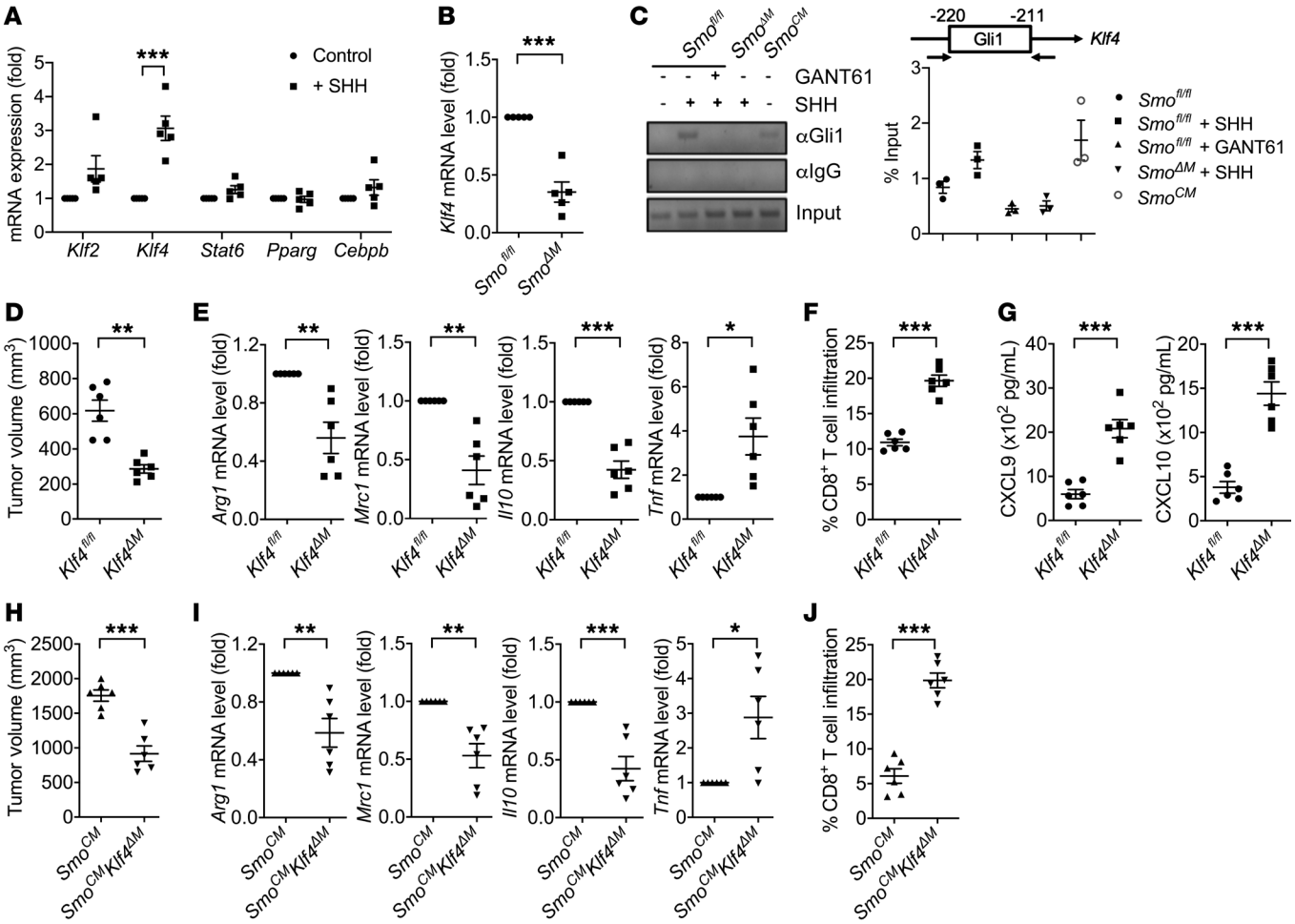

Figure 6. Hh-induced M2 TAM polarization and function are mediated by Klf4. (**A**) *Klf2*, *Klf4*, *Stat6*, *Pparg*, and *Cebpb* mRNA levels in control and SHH-treated macrophages were measured by qRT-PCR. Expression was normalized to *Actb* and compared with control. (**B**) *Klf4* mRNA levels in $Smo^{fl/fl}$ and $Smo^{\Delta M}$ TAMs were measured by qRT-PCR. Expression was normalized to reference gene *Actb* and compared with that of $Smo^{fl/fl}$. (**C**) Gli1 transcription factor binds to the *Klf4* promoter region as demonstrated by ChIP. Gli1 activity was inhibited using 5 μM GANT61 or constitutively activated using Smo^{CM} macrophages. (**D**) Tumor volumes of Hepa1-6 hepatoma cells inoculated s.c. in $Klf4^{fl/fl}$ and $Klf4^{\Delta M}$ mice on day 18 at sacrifice. (**E**) Expression of *Arg1*, *Mrc1*, *Il10*, and *Tnf* mRNAs in $Klf4^{fl/fl}$ and $Klf4^{\Delta M}$ TAMs was quantified by qRT-PCR. Expression was normalized to reference gene *Actb* and compared with that of $Klf4^{fl/fl}$ TAMs. (**F**) Percentages of tumor $CD8^+$ T cell infiltration into tumors from $Klf4^{fl/fl}$ and $Klf4^{\Delta M}$ mice. (**G**) CXCL9 and CXCL10 production by Smo^{CM} and $Smo^{CM}Klf4^{\Delta M}$ TAMs was measured by ELISA. (**H**) Tumor volumes of Hepa1-6 hepatoma cells inoculated s.c. in Smo^{CM} and $Smo^{CM}Klf4^{\Delta M}$ mice on day 18 at sacrifice. (**I**) Expression of *Arg1*, *Mrc1*, *Il10*, and *Tnf* mRNAs in Smo^{CM} and $Smo^{CM}Klf4^{\Delta M}$ TAMs was quantified by qRT-PCR. Expression was normalized to reference gene *Actb* and compared with that of Smo^{CM} TAMs. (**J**) Percentages of tumor $CD8^+$ T cell infiltration in tumors from Smo^{CM} and $Smo^{CM}Klf4^{\Delta M}$ mice. Values are the mean ± SEM of a minimum of 3 independent experiments. $^*P < 0.05$; $^{**}P < 0.005$; $^{***}P < 0.0005$. $n = 5$ biological replicates per group (**A** and **B**); $n = 3$ technical replicates per group (**C**); $n = 6$ biological replicates per group (**D**–**J**). Two-tailed Student's *t* test (**A**, **B**, **D**, and **J**).

ure 11, A–C) and increased $CD8^+$ T cell infiltration into the TME (Figure 6F). This was associated with increased production of CXCL9 and CXCL10 observed in $Smo^{CM}Klf4^{\Delta M}$ TAMs (Figure 6G), suggesting that Klf4 was mediating the downstream effects of Hh signaling on the suppression of CXCL9 and CXCL10 chemokine production. As previous reports have highlighted the antagonizing role of Klf4 in NF-κB signaling (33) and the importance of NF-κB in regulating Th1 chemokine production (34), we investigated whether SHH alters NF-κB p65 activity in macrophages. We found that, when *Klf4* was deleted, SHH treatment of macrophages did not significantly suppress NF-κB activity in the presence of IFN-γ (Supplemental Figure 11D). Collectively, these data suggest a critical role for Klf4 in M2 TAM polarization and function in vivo.

To further define that Klf4 works downstream of Hh to mediate M2 polarization in TAMs, we used $LysMcre^+Smo^C$ (referred to as Smo^{CM}) mice, which allows for constitutive activation of Hh signaling in Cre-expressing myeloid cells (30), and $LysMcre^+Smo^{CM}Klf4^{fl/fl}$ (referred to as $Smo^{CM}Klf4^{\Delta M}$) mice, which also had *Klf4* eliminated in the setting of a constitutively active Hh pathway. We observed that Smo^{CM} mice had accelerated tumor growth (Figure 6H), increased expression of Arg-1, CD206, IL-10, TGF-β1, and Chil3, and reduced levels of iNOS, TNF-α, and IL-6 (Figure 6I and Supplemental Figure 12), similar to what we observed in $Smo^{\Delta M}$ mice. Furthermore, Smo^{CM} had reduced $CD8^+$ T cell infiltration when compared with $Smo^{CM}Klf4^{\Delta M}$ mice (Figure 6J). Taken together, these results provide strong evidence to support that Klf4 works downstream of SHH

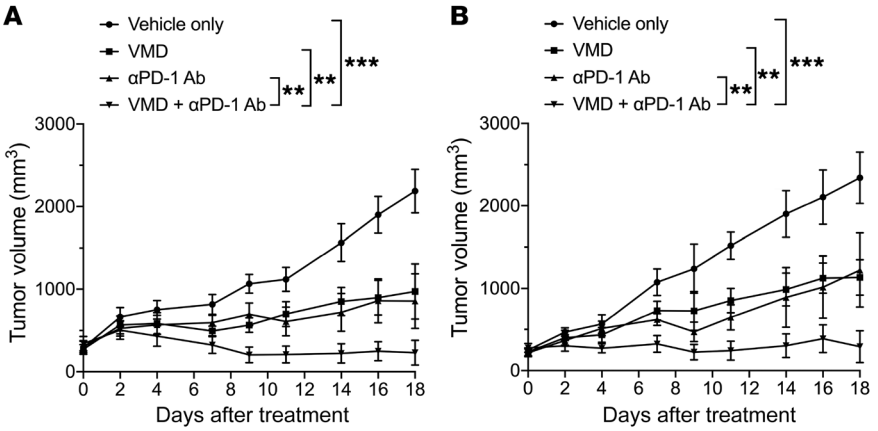

Figure 7. Hh inhibition and immune checkpoint blockade have synergistic antitumorigenic effects. (**A**) Tumor-bearing mice inoculated with 1 × 10^6 Hepa1-6 cells were treated with vehicle only (DMSO), vismodegib (VMD) (2 mg/mouse), anti–PD-1 antibody (200 μg/mouse), and a combination of VMD and anti–PD-1 antibody 3 times weekly for 3 weeks. (**B**) Tumor-bearing mice inoculated with 0.5 × 10^6 LLC1 cells were treated with vehicle only (DMSO), VMD (2 mg/mouse), anti–PD-1 antibody (200 μg/mouse), and a combination of VMD and anti–PD-1 antibody 3 times weekly for 3 weeks. $^{**}P < 0.005$; $^{***}P < 0.0005$. $n = 5$ biological replicates per group (**A** and **B**). Kruskal-Wallis test (**A** and **B**).

to induce M2 polarization of TAMs in vivo. These M2-polarized TAMs suppress CXCL9 and CXCL10 production by antagonizing NF-κB functions.

Hh inhibition and immune checkpoint blockade have synergistic antitumorigenic effects. Lastly, we investigated whether combination treatments of vismodegib (VMD), a small-molecule Hh inhibitor (35), and anti–PD-1 antibodies have synergistic effects in treating Hh-active cancers given that Hh signaling in TAMs promotes immunosuppression through interfering with $CD8^+$ T cell functions. To study this, we inoculated Hepa1-6 tumors in C57BL/6 mice and treated established tumors starting at day 10 with vehicle control, VMD only, anti–PD-1 antibody only, and combined VMD and anti–PD-1 antibody 3 times weekly for 3 weeks. We found that while VMD and PD-1 blockade both reduced tumorigenesis from control, combination treatments of VMD and PD-1 antibody decreased tumor growth most significantly ($P < 0.005$) (Figure 7A). We then repeated the same experiment with LLC1 cells and observed a significant ($P < 0.05$) synergistic effect of VMD and PD-1 blockade in reducing tumorigenesis (Figure 7B). Taken together, this suggests that combining Hh inhibitors with immune checkpoint blockade could provide additional therapeutic advantages in treating Hh-active human cancers.

Discussion

Here we showed that disruption of Hh signaling in myeloid cells impaired M2 polarization of TAMs and suppressed tumor growth. We further showed that tumor cells secrete SHH and that deletion of SHH in tumor cells led to impaired tumor growth and defective polarization of TAMs. We also demonstrated that Hh-induced functional polarization in TAMs suppressed intratumoral $CD8^+$ T cell infiltration through the inhibition of CXCL9 and CXCL10 production by TAMs, which is mediated by the transcription factor Klf4. Thus, our findings suggest a critical role for tumor-derived SHH in promoting TAM M2 polarization mediated by Klf4, and a mechanism by which TAM-mediated immunosuppression is accomplished by the inhibition of CXCL9/CXCL10–dependent $CD8^+$ T cell infiltration into the TME.

TAMs, representing 5%–10% of the tumor stromal mass in most solid tumors, play an important role in modulating tumor growth within the TME. Increased presence of M2 TAMs is correlated with poor clinical prognosis in a variety of human cancers (10–13). Previous studies have shown protumorigenic effects of TAMs on neoplastic progression (4–8). M2 TAMs can enhance tumor cell growth directly by promoting angiogenesis, cancer cell stemness, and chemotherapy resistance, and indirectly by inducing immune dysfunctions within the TME, resulting in immune evasion of cancer cells (4, 36). In HCC, TAMs have been shown to release various cytokines and signaling molecules, such as VEGF and matrix metalloproteinases (MMPs), to promote aberrant vascular formation and metastasis, while TAM-derived IL-6 can promote cancer stem cell growth via Stat3 signaling, resulting in chemotherapeutic resistance (37). Although a recent report has suggested a role for lactic acid in functional polarization of TAMs (14), the molecular pathways required for TAM M2 polarization in vivo remain largely unknown. A previous study has implicated the important role of Hh signaling in reprogramming the TME to facilitate tumorigenesis through TAMs in breast cancer (38). Our observations provided further evidence that the Hh signaling pathway in TAMs is critical for their M2 polarization to promote tumorigenesis. We also demonstrated that the Hh ligand SHH produced by tumor cells is responsible for driving immunosuppressive M2 polarization of TAMs within the TME to stimulate their own growth, suggesting the importance of communication between tumor cells and TAMs to promote tumor growth. Our findings further defined the role of Hh signaling and may provide an explanation for previous observations that Hh signaling is required and restricted to the stromal compartment during pancreatic carcinogenesis (19, 20).

Previous studies have suggested that M2-polarized TAMs can disrupt antitumor immune responses (4, 6). A recent study has also implicated macrophage PI3Kγ signaling in the suppression of $CD8^+$ T cell activation (39). Here we observed that Hh-polarized TAMs inhibited antitumor immunity by suppressing $CD8^+$ T cell infiltration into the TME, which is accomplished through downregulation of CXCL9 and CXCL10 production by TAMs. This is consistent with recent research demonstrating a nonredundant role for the CXCR3–CXCL9/CXCL10 axis for $CD8^+$ T cell trafficking to the tumor stroma (40). Additionally, elevated levels of CXCL9 and CXCL10 are positively correlated with intratumoral T cell infiltration and thus better prognosis in melanoma, serous ovarian cancer, and colorectal cancer patients (41, 42). Taken together, these observations support a notion that SHH plays a critical role in suppressing TAM-derived CXCL9- and CXCL10-mediated $CD8^+$ T cell infiltration into the TME in favor

of tumor progression. However, we cannot exclude the possibility that tumor-derived CXCL9 and CXCL10 may also play a role in regulating $CD8^+$ T cell infiltration, as a previous report has demonstrated that epigenetic silencing of CXCL9 and CXCL10 production from tumor cells significantly reduces $CD8^+$ T cell infiltration into the tumor stroma in ovarian cancers (43).

It is possible that Hh-induced M2-polarized TAMs can suppress effector T cell functions and promote tumorigenesis through other mechanisms. In our report, M2 TAMs express higher levels of Arg-1, IL-10, and TGF-β and lower levels of iNOS, IL-6, and TNF-α. Previous reports have highlighted that L-arginine depletion, mediated by TAM-derived Arg-1, can result in the failure to express CD3ζ chain in the T cell receptor complex, thus suppressing effector T cell activation (44). Furthermore, production of antiinflammatory cytokines, including IL-10 and TGF-β, can further interfere with cytotoxic $CD8^+$, Th1, and Th2 $CD4^+$ cell functions to promote a self-propagating immunosuppressive TME (45, 46). Lastly, TAMs and tumor-infiltrating myeloid cells can induce the dysfunction of tumor-infiltrating effector cells by expressing ligands for the inhibitory receptors programmed cell death protein 1 (PD-1) and cytotoxic T lymphocyte antigen-4 (CTLA-4) (47, 48). Taken together, this highlights the important role TAMs play in the TME, and further study is needed to investigate other immunologic mechanisms by which Hh-induced M2-polarized TAMs promote tumor growth.

Klf4 is a known mediator of macrophage M2 polarization. Klf4-deficient macrophages exhibit increased proinflammatory gene expression, enhanced bactericidal activity, and delayed wound healing (49), consistent with a more M1 phenotype. Here we provide what is, to our knowledge, the first evidence that the downstream Hh pathway transcription factor Gli1 regulates Klf4 expression. Subsequently, Klf4 mediates the downstream effects of Hh signaling in M2 polarization of TAMs and their secretion of CXCL9 and CXCL10 to modulate $CD8^+$ T cell trafficking to the tumor site. Our finding is consistent with a previous report that Klf4 deficiency in myeloid cells is associated with increased $CD8^+$ T cell infiltration in prostate cancer (50). Additionally, we provided further evidence showing that Klf4 interferes with NF-κB signaling in macrophages, resulting in reduced Th1 chemokine production. Collectively, our data showed the critical role of the Hh-Gli1-Klf4 signaling cascade in promoting TAM M2 polarization and intratumoral immunosuppression.

Lastly, our data indicated that inhibition of Hh signaling is an effective way of reversing the protumorigenic phenotype of M2 TAMs, resulting in increased $CD8^+$ T cell trafficking into the TME. Though targeted inhibition of Hh signaling has been proven to be effective in the treatment of many types of human cancers (16, 51), few reports have investigated the effects of Hh inhibition on tumor-infiltrating T cells or its potential to be combined with immune checkpoint blockade inhibitors. Here we showed that combination treatments of the Hh pathway inhibitor VMD and PD-1 blockade have synergistic effects in suppressing tumor growth. As more therapies are starting to target various immunosuppressive components of the TME, this report illustrates the important therapeutic potential of Hh inhibitors in modulating antitumor immune responses. Further studies are needed to develop and investigate novel immunotherapeutic strategies based on targeting of SHH and its downstream signaling pathway to augment antitumor immune responses.

In conclusion, we have identified an important role for tumor cell–derived SHH in acting directly on TAMs to promote their M2 polarization and tumor growth mediated by the transcription factor Klf4. We further demonstrated that Hh-dependent M2 polarization of TAMs suppressed $CD8^+$ T cell infiltration into the TME via reduction of CXCL9 and CXCL10. Our findings may provide important insights into the development of novel immunotherapeutic strategies for treating cancer.

Methods

Animals. Eight- to ten-week-old male C57BL/6 mice were purchased from the National Cancer Institute (Frederick, Maryland, USA). STOCK-Smo^{tm2Amc}/J ($Smo^{fl/fl}$), $Gt(ROSA)26Sor^{tm1(Smo/EYFP)Amc}/J$ (Smo^{C}), $Lyz2^{tm1(cre)Ifo}/J$ (*LysMcre*), and $Abcb4^{tm1Bor}$ ($Mdr2^{-/-}$) mice were purchased from The Jackson Laboratory. $Klf4^{tm1Khk}$ *Mmmh* ($Klf4^{fl/fl}$) mice were purchased from Mutant Mouse Resource and Research Center. $Smo^{fl/fl}$ and Smo^{C} mice were backcrossed with C57BL/6 mice in-house for at least 9 generations. Backcrossed $Smo^{fl/fl}$, Smo^{C}, and $Klf4^{fl/fl}$ mice were crossed with *LysMcre* mice to generate $LysMcre^{+}Smo^{fl/fl}$ mice (referred to herein as $Smo^{\Delta M}$), $LysMcre^{+}$*Smo-M2*^{C} mice (referred to herein as Smo^{CM}), and $LysMcre^{+}Klf4^{fl/fl}$ mice (referred to herein as $Klf4^{\Delta M}$) on a pure C57BL/6 background. Control mice were $LysMcre^{-}Smo^{fl/fl}$ (referred to herein as $Smo^{fl/fl}$) or $LysMcre^{-}Klf4^{fl/fl}$ (referred to herein as $Klf4^{fl/fl}$). $LysMcre^{+}Smo^{C}Klf4^{fl/fl}$ (referred to herein as $Smo^{CM}Klf4^{fl/fl}$) mice were generated by crossing $LysMcre^{+}Klf4^{fl/fl}$ mice with *Smo-M2*^{C} mice. $LysMcre^{+}Smo^{fl/fl}Mdr2^{-/-}$ (referred to herein as $Smo^{\Delta M}Mdr2^{-/-}$) mice and their pertinent control $LysMcre^{-}Smo^{fl/fl}Mdr2^{-/-}$ mice (referred to herein as $Smo^{fl/fl}Mdr2^{-/-}$) were generated by crossing $LysMcre^{+}Smo^{fl/fl}$ mice with $Mdr2^{-/-}$ mice.

Cell lines and reagents. Unless otherwise stated, all cell culture media were obtained from Life Technologies. Hepa1-6 (CRL-1830), LLC1 (CRL-1642), and 293T (CRL-11268) were obtained from the ATCC. Cell lines were cultured in DMEM supplemented with 10% FBS, 100 IU/mL penicillin, and 100 IU/mL streptomycin. Peritoneal macrophages collected from mouse peritoneal cavity and TAMs and leukocytes collected from tumor samples were cultured in complete RPMI 1640 medium supplemented with 10% FBS, 1 mM sodium pyruvate, 0.1 mM nonessential amino acids, 50 μM 2-ME, 2 mM L-glutamine, 100 IU/mL penicillin, and 100 IU/mL streptomycin. Recombinant mouse SHH-N ligand for in vitro treatment of macrophages was purchased from R&D Systems.

Tumor models. Hepa1-6 hepatoma (3×10^6) or LLC1 lung carcinoma (1×10^6) cells were injected s.c. into each mouse in the right hind leg region in 100 μL PBS with a 27-gauge needle syringe. For treatments, beginning 10 days after injection of tumor cells, mice were injected i.p. with 100 μL (2 mg/mouse) of vismodegib (VMD; Selleck Chemicals), 200 μL (200 μg/mouse) anti–PD-1 antibody, a combination of VMD and PD-1 antibody, or DMSO as a vehicle control 3 times weekly until humane endpoints were reached.

Both male and female mice were used. Mice were 6–8 weeks of age. There was no systematic means of randomization of mice. Three-digit codes identified the mice, and the experiment was carried out blindly throughout. To estimate the volume of the growing tumor mass, diameters of both the length (*a*) and the width (*b*) of the mass were measured every 3–4 days, after which the tumor volume (*V*) was calculated according to the formula $V = ab^2/2$, as described previously (52). When experimental endpoints were met or when the longer

axis of each tumor was greater than 20 mm in diameter, all of the mice were euthanized according to NIH guidelines. Tumors were resected and transferred to 2 mL RPMI 1640 medium on ice. Tumor size (millimeters) was measured with a ruler. The tumors from all experiments were then processed for FACS analysis or sorting on the same day or frozen in OCT compound (VWR) for cryosectioning.

Generation of Shh-KO cell lines using CRISPR/Cas9 technology. Synthesized sgRNA oligonucleotides (Integrated DNA Technologies) were annealed and subcloned into lentiviral expression vector LentiCRISPR-v2 (Addgene 52961, deposited by F. Zhang) for sgRNA expression (53). Lentivirus was produced by triple transfection of 293T cells with the sgRNA expression LentiCRISPR-v2 vector and the packaging plasmids pCMV-VSV-G (Addgene 8454, deposited by R. Weinberg) and pCMV-dR8.2 dvpr (Addgene, deposited by R. Weinberg) at a 1:1:2 ratio. Transfection was performed using Lipofectamine 3000 (Thermo Fisher Scientific) as recommended by the manufacturer. The viral supernatant was collected 48 hours after transfection and filtered through a 0.45-μm filter. Mouse hepatoma Hepa1-6 and Lewis lung carcinoma LLC1 cells were transduced with lentivirus in the presence of 8 μg/mL Polybrene (Sigma-Aldrich) for 8 hours. Five days after transduction, transduced cells underwent single-cell dilution and were grown in the presence of 0.8 mg/mL G418 (Thermo Fisher Scientific). Knockout status of expanded single-cell clones was confirmed by immunoblotting and ELISA assayed for SHH. Forward sgRNA sequences for CRISPR/Cas9 knockout were as follows: SHH sgRNA#1, 5′-CCGCGACGAAGGCGCCAAGA-3′; SHH sgRNA#2, 5′-CTTCTACGTGATCGAGACGC-3′; nontargeting control, 5′-AAGTCTATGCGGGGCTCGTA-3′.

Reporter assays. Lentivirus was produced by triple transfection of 293T cells with the pGreenFire-Gli reporter plasmid (System Biosciences) and the packaging plasmids as described above. pGreenFire-Gli encodes 4 Gli transcription response element sites upstream of GFP and luciferase genes. Mouse bone marrow–derived macrophages (BMDMs) were transduced with lentivirus in the presence of 8 μg/mL Polybrene (Sigma-Aldrich) for 8 hours. Cells were then left untreated or treated with 10 ng/mL SHH for 12 hours. GFP activity was then assessed with FACS 48 hours after transduction.

Immunoblotting. Cells were lysed in 1% Triton X-100 in TBS, pH 7.6, with Roche complete protease inhibitor for 30 minutes on ice followed by pelleting of insoluble material by centrifugation. Lysates were heated to 95°C in SDS sample buffer with 50 mM DTT for 10 minutes, separated by SDS-PAGE, and transferred to nitrocellulose membrane (Millipore). Membranes were blocked in 5% milk in TBS plus 0.1% Tween-20 and probed with rabbit anti–mouse SHH and rabbit anti–β-actin antibodies (Cell Signaling Technology). Reactive bands were visualized using West Pico (Thermo Fisher Scientific).

Measurement of SHH. One million Hepa1-6/LLC1 *Shh*-WT or *Shh*-KO cells were plated in 96-well plates for 24 hours. Concentration of SHH protein in 200 μL supernatant was assayed by ELISA according to RayBiotech's instructions (ELM-ShhN-1). The detection threshold for the assay was 5 pg/mL.

Antibodies and flow cytometry analysis. The list of antibodies used in this study is provided in Supplemental Table 1. Titration was used to determine the optimal concentration of each antibody before each experiment. Cell suspensions were stained with relevant antibodies at 4°C for 15 minutes in PBS with 2% heat-inactivated FBS and 0.1% sodium azide, washed twice, and analyzed with a FACSCanto flow cytometer (BD Biosciences) using FlowJo Software (Tree Star).

Preparation of single-cell suspensions from tumors. The isolation of TAMs and leukocytes was previously described (40) and was slightly modified for this study. Briefly, tumors were excised from mice and digested with 50 U/mL collagenase I, 100 U/mL collagenase IV, and 50 U/mL DNase I (Worthington Biochemical) for 1 hour at 37°C, crushed gently to homogenize the mass, and then filtered through a 100-μm cell strainer (Becton Dickinson). Red blood cells were lysed with ACK lysis buffer followed by washing with FACS buffer. Leukocytes were further separated from contaminating tumor cells by centrifugation over a 40%–75% Ficoll Paque (Life Technologies) gradient at 600 *g* for 30 minutes at room temperature. For sorting of TAMs, Ficoll-enriched leukocytes were stained with anti-F4/80, anti-CD11b, anti-Ly6G, and anti-Ly6C antibodies and purified by FACS for $F4/80^+CD11b^+Ly6G^-Ly6C^-$ cells.

Isolation of BMDMs. To prepare macrophages, mice were sacrificed and disinfected with 70% ethanol. Both lower extremities were excised, and the long bones — femur and tibia — were separated from muscular layers and placed in RPMI medium. To extract BMDMs, 10 mL RPMI medium was used to flush out each bone using a 25-gauge needle, and cells were gently dissociated by pipetting. A 70-μm nylon BD Falcon cell strainer was placed atop a 50-mL BD Falcon tube, and the suspension was filtered into the 50-mL tube. The resultant suspension was centrifuged at 1500 rpm for 5 minutes. The supernatant was then aspirated. ACK lysis buffer (5 mL) was then added, and the contents were incubated for 2 minutes at room temperature. To quench the lysis reaction, 10 mL RPMI was added. The contents were then centrifuged, and the cells were washed 2 additional times with 1× HBSS. The cells were plated at 1×10^6 cells per well in a sterile 6-well tissue culture plate in 2 mL BMDM culture medium plus 10 ng/mL M-CSF to obtain mature BMDMs. On day 2, supernatants were aspirated and replenished with fresh culture medium with M-CSF. On day 5, 2 mL fresh culture medium with M-CSF was added.

Intracellular cytokine staining. TAMs from tumor-bearing mice and peritoneal macrophages were restimulated with 50 ng/mL lipopolysaccharide for 5 hours in the presence of 5 μg/mL brefeldin A (Invitrogen). After staining with cell surface markers, the cells were fixed and permeabilized with a Cytoperm/Cytofix kit (BD Biosciences) for 20 minutes and incubated with anti–Arg-1 antibodies for 30 minutes. The cells were washed twice with Permeabilization Buffer (Thermo Fisher Scientific) and analyzed with a FACSCanto flow cytometer.

Measurement of cytokines and chemokines. One million peritoneal macrophages or TAMs were cultured in flat-bottomed 96-well plates for 24 hours, and culture supernatants were assayed for the secretion of TNF-α, IL-6, and IL-10 by an Inflammatory Cytometric Bead Array kit (BD Biosciences). Secretion of TGF-β and Chil3 was measured with ELISA kits purchased from RayBiotech.

Real-time PCR. Total RNA was isolated from sorted mouse macrophages and TAMs using Trizol reagent according to the manufacturer's recommendations (Invitrogen). Genomic DNA contamination was eliminated by treatment with DNase I (Life Technologies). Reverse transcription was performed with the Superscript First-Strand Synthesis System (Promega). RNA samples (0.5–1 μg) were converted to first-strand cDNAs using random and oligo-$(dT)_{15}$ primer mixture (1:1). The cDNA samples were diluted 1:10 in water and analyzed in duplicate using SYBR Green Real-Time PCR Master Mixes (Bio-Rad). SYBR Green PCR conditions were 1 cycle of 50°C for 2 minutes, 1 cycle of 95°C for 10 minutes, and 40 cycles of 95°C for 15 seconds, 60°C

for 60 seconds by a model CFX96 Touch Real-Time PCR Detection System (Bio-Rad). Primer sequences are summarized in Supplemental Table 2. Relative gene expression levels of each respective gene were calculated using the threshold cycle ($2^{-\Delta\Delta CT}$) method and normalized to β-actin (54).

In vivo blockade of CXCR3. For the in vivo CXCR3 blocking experiments, mice were injected i.p. with 200 μg anti-CXCR3 mAb (CXCR3-173) or polyclonal Armenian hamster IgG (BioXCell) concurrently with tumor inoculation, then every 3 days until an endpoint was reached.

Chromatin immunoprecipitation. ChIP assays were performed as previously described (48). Briefly, 1×10^7 cells were untreated, treated with 100 pg/mL SHH for 3 days, or treated with 100 pg/mL SHH plus 5 μM GANT61 for 3 days before cross-linking for 10 minutes with 1% formaldehyde. Antibody recognizing Gli1 was purchased from Novus Biologicals. Normal rabbit IgG (Cell Signaling Technology) was used as negative control. *Klf4* promoter RT-PCR was performed with the specific primers flanking the Gli1-binding site (sense, 5′-CGTGCGCG-GAGTTTGTTTAT-3′; antisense, 5′-TAACTTCTCGCTCGCTTGCT-3′). PCR products were analyzed with agarose gel electrophoresis.

Histology and imaging. Cryostat sections (10 μm) were dried, fixed in cold acetone, and incubated for 30 minutes in blocking buffer (10% goat or rabbit serum in PBS). Slides were then incubated with primary antibody diluted in 2% serum in PBS at room temperature in a humidity chamber for 30 minutes. After washing 3 times with 2% serum diluted in PBS each for 5 minutes, slides were incubated with secondary antibody diluted in 2% serum at room temperature for 30 minutes. Nuclei were stained with 100 ng/mL Hoechst in PBS and incubated for 15 minutes at room temperature in the dark. Slides were washed 2 times with PBS, mounted with Fluoromount (SouthernBiotech), and imaged on a Nikon C2 confocal microscope. 405-nm, 488-nm, and 647-nm lasers were used to excite Hoechst-, Alexa Fluor 488–, and Alexa Fluor 647–labeled antigens, respectively. Sequential acquisitions of the multicolor images were used to avoid cross-excitation, and images were overlaid with Nikon NIS-Element Confocal Microscope Imaging Software.

For immunohistochemical staining, acetone-fixed slides were washed 2 times with PBS and quenched with hydrogen peroxide for 10 minutes. A protein block was then applied to block nonspecific background binding. After washing with PBS, slides were incubated with primary antibody overnight at 4°C. Biotinylated anti-rabbit secondary antibody (Abcam) was applied for 10 minutes the next day after washing with PBS. Slides were then incubated with streptavidin peroxidase for 10 minutes and developed with DAB chromogen (Abcam). Slides were washed 2 times with PBS, mounted with Fluoromount, and imaged on a Nikon Eclipse Ti microscope. For H&E staining, liver tumors were fixed in 10% formalin after harvesting. The sectioning and H&E staining were performed by the Pathology Laboratory, Duke University Medical Center. Slide imaging and tumor measurement were conducted using Nikon Eclipse Ti and the associated NIS-Elements software.

Chemotaxis assay. Chemotaxis of murine $CD8^+$ T cells was assayed in 24-well plates (5-μm-pore-size Transwell insert with polycarbonate membranes; Corning). Medium alone (RPMI 1640 plus 10% FBS) or supernatants from macrophages were placed at the bottom of the triplicate wells. Murine T cell migration was assessed with medium, 50 U/mL IFN-γ–treated supernatant alone, supernatant plus 10 μg/mL anti-CXCL9 neutralizing antibodies, and/or 10 μg/mL anti-CXCL10 neutralizing antibodies (R&D Systems). $CD8^+$ cells (5×10^5) from C57BL/6 mouse spleen and lymph nodes were purified with anti-CD8a beads (Miltenyi Biotec) and then fluorescently labeled with CFSE, placed on the Transwell insert, and incubated at 37°C for 24 hours. Cells in the bottom chamber were enumerated by flow cytometry. Spontaneous migration was subtracted from all conditions, and data were reported as chemotactic index. Chemotactic index = (migrated cells – spontaneous migrated cells)/total T cells plated in Transwell × 100%.

Statistics. Results are expressed as mean ± SEM. Comparison between groups was performed by Kruskal-Wallis, Wilcoxon-Mann-Whitney, and 2-tailed Student's *t* test. All statistical analyses were performed with JMP version 12 software (SAS Software). *P* values less than 0.05 are considered to be significant.

Study approval. All experiments were performed according to protocols approved by the IACUC of Duke University.

Author contributions

AJP designed and performed the experiments, analyzed the data, and wrote the manuscript. AL, XW, RD, and DH assisted in performing the experiments. BH and XH contributed essential ideas and discussion. XH and YY assisted in designing the experiments, supervised the work, and wrote the manuscript.

Acknowledgments

This work was supported by NIH grants CA136934, CA186973, and CA193167 (to YY). AJP is supported by NIH predoctoral fellowship CA213799.

Address correspondence to: Yiping Yang, Division of Hematology, The Ohio State University Wexner Medical Center, 508 BRT, 460 W. 12th Avenue, Columbus, Ohio 43210, USA. Phone: 614.685.0643; Email: yiping.yang2@osumc.edu.

1. Ginhoux F, Jung S. Monocytes and macrophages: developmental pathways and tissue homeostasis. *Nat Rev Immunol*. 2014;14(6):392–404.
2. Sica A, Mantovani A. Macrophage plasticity and polarization: in vivo veritas. *J Clin Invest*. 2012;122(3):787–795.
3. Xue J, et al. Transcriptome-based network analysis reveals a spectrum model of human macrophage activation. *Immunity*. 2014;40(2):274–288.
4. Qian BZ, Pollard JW. Macrophage diversity enhances tumor progression and metastasis. *Cell*. 2010;141(1):39–51.
5. Condeelis J, Pollard JW. Macrophages: obligate partners for tumor cell migration, invasion, and metastasis. *Cell*. 2006;124(2):263–266.
6. Murdoch C, Muthana M, Coffelt SB, Lewis CE. The role of myeloid cells in the promotion of tumour angiogenesis. *Nat Rev Cancer*. 2008;8(8):618–631.
7. Franklin RA, et al. The cellular and molecular origin of tumor-associated macrophages. *Science*. 2014;344(6186):921–925.
8. Noy R, Pollard JW. Tumor-associated macrophages: from mechanisms to therapy. *Immunity*. 2014;41(1):49–61.
9. Heusinkveld M, van der Burg SH. Identification and manipulation of tumor associated macrophages in human cancers. *J Transl Med*. 2011;9:216.
10. Kim KJ, Wen XY, Yang HK, Kim WH, Kang GH. Prognostic implication of M2 macrophages are determined by the proportional balance of tumor associated macrophages and tumor infiltrating lymphocytes in microsatellite-unstable gastric carcinoma. *PLoS One*. 2015;10(12):e0144192.
11. Zhang M, et al. A high M1/M2 ratio of tumor-

associated macrophages is associated with extended survival in ovarian cancer patients. *J Ovarian Res*. 2014;7:19.
12. Edin S, et al. The distribution of macrophages with a M1 or M2 phenotype in relation to prognosis and the molecular characteristics of colorectal cancer. *PLoS One*. 2012;7(10):e47045.
13. Cui R, Yue W, Lattime EC, Stein MN, Xu Q, Tan XL. Targeting tumor-associated macrophages to combat pancreatic cancer. *Oncotarget*. 2016;7(31):50735–50754.
14. Colegio OR, et al. Functional polarization of tumour-associated macrophages by tumour-derived lactic acid. *Nature*. 2014;513(7519):559–563.
15. Theunissen JW, de Sauvage FJ. Paracrine Hedgehog signaling in cancer. *Cancer Res*. 2009;69(15):6007–6010.
16. Hanna A, Shevde LA. Hedgehog signaling: modulation of cancer properies and tumor mircroenvironment. *Mol Cancer*. 2016;15:24.
17. Gupta S, Takebe N, Lorusso P. Targeting the Hedgehog pathway in cancer. *Ther Adv Med Oncol*. 2010;2(4):237–250.
18. O'Toole SA, et al. Hedgehog overexpression is associated with stromal interactions and predicts for poor outcome in breast cancer. *Cancer Res*. 2011;71(11):4002–4014.
19. Yauch RL, et al. A paracrine requirement for hedgehog signalling in cancer. *Nature*. 2008;455(7211):406–410.
20. Tian H, et al. Hedgehog signaling is restricted to the stromal compartment during pancreatic carcinogenesis. *Proc Natl Acad Sci U S A*. 2009;106(11):4254–4259.
21. Long F, Zhang XM, Karp S, Yang Y, McMahon AP. Genetic manipulation of hedgehog signaling in the endochondral skeleton reveals a direct role in the regulation of chondrocyte proliferation. *Development*. 2001;128(24):5099–5108.
22. Clausen BE, Burkhardt C, Reith W, Renkawitz R, Förster I. Conditional gene targeting in macrophages and granulocytes using LysMcre mice. *Transgenic Res*. 1999;8(4):265–277.
23. Giese MA, Hind LE, Huttenlocher A. Neutrophil plasticity in the tumor microenvironment. *Blood*. 2019;133(20):2159–2167.
24. Mauad TH, et al. Mice with homozygous disruption of the mdr2 P-glycoprotein gene. A novel animal model for studies of nonsuppurative inflammatory cholangitis and hepatocarcinogenesis. *Am J Pathol*. 1994;145(5):1237–1245.
25. Pikarsky E, et al. NF-κB functions as a tumour promoter in inflammation-associated cancer. *Nature*. 2004;431(7007):461–466.
26. Katzenellenbogen M, et al. Molecular mechanisms of liver carcinogenesis in the mdr2-knockout mice. *Mol Cancer Res*. 2007;5(11):1159–1170.
27. Groom JR, Luster AD. CXCR3 ligands: redundant, collaborative and antagonistic functions. *Immunol Cell Biol*. 2011;89(2):207–215.
28. Lawrence T, Natoli G. Transcriptional regulation of macrophage polarization: enabling diversity with identity. *Nat Rev Immunol*. 2011;11(11):750–761.
29. Hooper JE, Scott MP. Communicating with Hedgehogs. *Nat Rev Mol Cell Biol*. 2005;6(4):306–317.
30. Jeong J, Mao J, Tenzen T, Kottmann AH, McMahon AP. Hedgehog signaling in the neural crest cells regulates the patterning and growth of facial primordia. *Genes Dev*. 2004;18(8):937–951.
31. Lauth M, Bergström A, Shimokawa T, Toftgård R. Inhibition of GLI-mediated transcription and tumor cell growth by small-molecule antagonists. *Proc Natl Acad Sci U S A*. 2007;104(20):8455–8460.
32. Katz JP, et al. The zinc-finger transcription factor Klf4 is required for terminal differentiation of goblet cells in the colon. *Development*. 2002;129(11):2619–2628.
33. Liao X, et al. Krüppel-like factor 4 regulates macrophage polarization. *J Clin Invest*. 2011;121(7):2736–2749.
34. Liu T, Zhang L, Joo D, Sun SC. NF-κB signaling in inflammation. *Signal Transduct Target Ther*. 2017;2:17023.
35. Stanton BZ, Peng LF. Small-molecule modulators of the Sonic Hedgehog signaling pathway. *Mol Biosyst*. 2010;6(1):44–54.
36. Biswas SK, Mantovani A. Macrophage plasticity and interaction with lymphocyte subsets: cancer as a paradigm. *Nat Immunol*. 2010;11(10):889–896.
37. Wan S, Kuo N, Kryczek I, Zou W, Welling TH. Myeloid cells in hepatocellular carcinoma. *Hepatology*. 2015;62(4):1304–1312.
38. Hanna A, et al. Inhibition of Hedgehog signaling reprograms the dysfunctional immune microenvironment in breast cancer. *Oncoimmunology*. 2019;8(3):1548241.
39. Kaneda MM, et al. PI3Kγ is a molecular switch that controls immune suppression. *Nature*. 2016;539(7629):437–442.
40. Mikucki ME, et al. Non-redundant requirement for CXCR3 signalling during tumoricidal T-cell trafficking across tumour vascular checkpoints. *Nat Commun*. 2015;6:7458.
41. Harlin H, et al. Chemokine expression in melanoma metastases associated with $CD8^+$ T-cell recruitment. *Cancer Res*. 2009;69(7):3077–3085.
42. Kistner L, Doll D, Holtorf A, Nitsche U, Janssen KP. Interferon-inducible CXC-chemokines are crucial immune modulators and survival predictors in colorectal cancer. *Oncotarget*. 2017;8(52):89998–90012.
43. Peng D, et al. Epigenetic silencing of TH1-type chemokines shapes tumour immunity and immunotherapy. *Nature*. 2015;527(7577):249–253.
44. Rodriguez PC, Quiceno DG, Ochoa AC. L-arginine availability regulates T-lymphocyte cell-cycle progression. *Blood*. 2007;109(4):1568–1573.
45. Oh SA, Li MO. TGF-β: guardian of T cell function. *J Immunol*. 2013;191(8):3973–3979.
46. Ruffell B, et al. Macrophage IL-10 blocks $CD8^+$ T cell-dependent responses to chemotherapy by suppressing IL-12 expression in intratumoral dendritic cells. *Cancer Cell*. 2014;26(5):623–637.
47. Lin H, et al. Host expression of PD-L1 determines efficacy of PD-L1 pathway blockade-mediated tumor regression. *J Clin Invest*. 2018;128(2):805–815.
48. Curiel TJ, et al. Blockade of B7-H1 improves myeloid dendritic cell-mediated antitumor immunity. *Nat Med*. 2003;9(5):562–567.
49. Liao X, et al. Krüppel-like factor 4 regulates macrophage polarization. *J Clin Invest*. 2011;121(7):2736–2749.
50. Barakat DJ, Suresh R, Barberi T, Pienta KJ, Simons BW, Friedman AD. Absence of myeloid Klf4 reduces prostate cancer growth with pro-atherosclerotic activation of tumor myeloid cells and infiltration of CD8 T cells. *PLoS One*. 2018;13(1):e0191188.
51. Cortes JE, et al. Randomized comparison of low dose cytarabine with or without glasdegib in patients with newly diagnosed acute myeloid leukemia or high-risk myelodysplastic syndrome. *Leukemia*. 2019;33(2):379–389.
52. Faustino-Rocha A, et al. Estimation of rat mammary tumor volume using caliper and ultrasonography measurements. *Lab Anim (NY)*. 2013;42(6):217–224.
53. Cong L, et al. Multiplex genome engineering using CRISPR/Cas systems. *Science*. 2013;339(6121):819–823.
54. Livak KJ, Schmittgen TD. Analysis of relative gene expression data using real-time quantitative PCR and the $2^{-\Delta\Delta CT}$ method. *Methods*. 2001;25(4):402–408.